Mon. Not. R. Astron. Soc. **333,** 809–824 (2002)

Multiwavelength observations of serendipitous *Chandra* X-ray sources in the field of A 2390

C. S. Crawford,[1★] P. Gandhi,[1] A. C. Fabian,[1] R. J. Wilman,[1,2] R. M. Johnstone,[1] A. J. Barger[3,4]† and L. L. Cowie[3]‡

[1]*Institute of Astronomy, Madingley Road, Cambridge CB3 0HA*
[2]*Leiden Observatory, PO Box 9513, 2300 RA Leiden, The Netherlands*
[3]*Institute for Astronomy, 2680 Woodlawn Drive, Honolulu HI 96822, USA*
[4]*Department of Astronomy, University of Wisconsin-Madison, 475 N Charter Street, Madison, WI 53706, USA*

Accepted 2002 February 21. Received 2002 February 12; in original form 2001 June 6

ABSTRACT

We present optical spectra and near-infrared imaging of a sample of 31 serendipitous X-ray sources detected in the field of *Chandra* observations of the A 2390 cluster of galaxies. The sources have 0.5–7 keV fluxes of $(0.6–8) \times 10^{-14}$ erg cm^{-2} s^{-1} and lie around the break in the 2–10 keV source counts. They are therefore typical of sources dominating the X-ray Background in that band. 12 of the 15 targets for which we have optical spectra show emission lines at a range of line luminosities, and half of these show broad lines. These active galaxies and quasars have soft X-ray spectra. Including photometric redshifts and published spectra, we have redshifts for 17 of the sources, ranging from $z \sim 0.2$ up to $z \sim 3$, with a peak between $z = 1–2$. 10 of our sources have hard X-ray spectra indicating a spectral slope flatter than that of a typical unabsorbed quasar. Two hard sources that are gravitationally lensed by the foreground cluster are obscured quasars, with intrinsic 2–10 keV luminosities of $(0.2–3) \times 10^{45}$ erg s^{-1}, and absorbing columns of $N_{\rm H} > 10^{23}$ cm^{-2}. Both of these sources were detected in the mid-infrared by ISOCAM on the *Infrared Space Observatory*, which when combined with radiative transfer modelling leads to the prediction that the bulk of the reprocessed flux emerges at $\sim 100\,\mu$m.

Key words: galaxies: active – diffuse radiation – infrared: galaxies – X-rays: galaxies.

1 INTRODUCTION

The cosmic X-ray Background (XRB) in the energy range 0.5–7 keV has now been mostly resolved into point sources. About 90 per cent of the 0.5–2 keV soft XRB has been resolved with *ROSAT* (Hasinger et al. 1998; Lehmann et al. 2001), and now *Chandra* has also resolved more than 80 per cent of the harder 2–7 keV band (Mushotzky et al. 2000; Barger et al. 2001; Brandt et al. 2001; Giacconi et al. 2001; Hornschemeier et al. 2001; Tozzi et al. 2001). Follow-up work on the deep fields which gave these *Chandra* results is proceeding, but full details including redshifts are published for only about a half, or less, of the brighter sources detected. The determination of complete details of the optically and X-ray faintest sources is likely to take some time.

The harder 2–7 keV X-ray source counts flatten below a flux of about 10^{-14} erg cm^{-2} s^{-1} (Mushotzky et al. 2000; Giacconi et al. 2001), which means that much of the information about the origin of the bulk of the XRB is contained in sources around that flux level. Deep X-ray observations are not required to detect such sources, and several tens are routinely found as serendipitous sources in *Chandra* exposures of 10–20 ks on other targets. Indeed, for a given total exposure time, more such sources are found from say 10 separate 20-ks exposures than will be found from one deep 200-ks exposure, due to the flatter faint source counts.

We have begun a programme (Fabian et al. 2000; Crawford et al. 2002) of studying the serendipitous sources in our *Chandra* cluster fields, which have typical exposures of about 20 ks. At this flux level the optically identified sources are associated roughly equally with normal quasars, optically bright galaxies and optically faint galaxies (Mushotzky et al. 2000). The latter often appear to be of early-type (Barger et al. 2001). All are plausibly powered by active galactic nuclei (AGN), but the harder sources are mostly obscured by significant intrinsic absorption columns ($\sim 10^{21}$–10^{23} cm^{-2}). Reddening by dust associated with this absorbing gas can render

★E-mail: csc@ast.cam.ac.uk
† Hubble Fellow and Chandra Fellow at Large.
‡ Visiting Astronomer, W. M. Keck Observatory, jointly operated by the California Institute of Technology and the University of California.

Table 1. Serendipitous X-ray sources in the field of the cluster A2390.

Name	Seq. No. [Chip]	RA_X (J2000)	$\Delta\alpha_X$ ($''$)	DEC_X (J2000)	$\Delta\delta_X$ ($''$)	WAV (cts)	(err)	Sig	0.5–7 keV (cts)	(err)	0.5–2 keV (cts)	(err)	2–7 keV (cts)	(err)	S/H	(err)	PSF ratio
A1	800008 [I2]	21:52:34.92	(1.2)	+17:38:10.0	(1.5)	22.80	(8.83)	7.97	55.76	(8.81)	36.39	(6.77)	18.55	(5.58)	1.96	(0.69)	1.11
A2	800008 [I3]	21:52:44.42	(1.6)	+17:43:54.6	(1.6)	8.01	(4.91)	4.05	15.59	(4.83)	9.37	(3.52)	7.32	(3.48)	1.28	(0.77)	1.02
	800009 [I3]	–	–	–	–	–	–	–	<8.76	–	<6.07	–	<5.93	–	–	–	–
A3	800008 [I3]	–	–	–	–	–	–	–	<5.53	–	<2.94	–	<4.72	–	–	–	–
	800009 [I3]	21:52:55.76	(0.7)	+17:44:33.6	(0.5)	11.17	(3.91)	4.95	12.62	(3.92)	8.33	(3.11)	<4.76	–	>1.74	–	0.56
A4	800008 [I3]	–	–	–	–	–	–	–	<4.63	–	<4.58	–	<0.41	–	–	–	–
	800009 [I3]	21:53:00.91	(0.4)	+17:44:51.9	(0.7)	8.94	(3.42)	4.20	11.46	(3.58)	7.88	(2.90)	<4.18	–	>1.89	–	0.48
A5	800009 [I2]	21:53:04.88	(0.6)	+17:38:33.3	(0.5)	13.04	(4.07)	5.73	15.76	(4.20)	13.54	(3.79)	<3.56	–	>3.80	–	0.82
A6	800008 [S3]	21:53:20.69	(0.1)	+17:41:19.2	(0.1)	40.76	(6.47)	19.22	41.34	(6.48)	29.19	(5.44)	12.18	(3.51)	2.40	(0.82)	1.10
	800009 [S3]	21:53:20.68	(0.1)	+17:41:19.1	(0.1)	57.74	(7.79)	23.77	59.77	(7.79)	50.51	(7.15)	9.23	(3.09)	5.47	(1.99)	1.11
A7	800008 [S3]	21:53:22.54	(0.2)	+17:40:18.2	(0.1)	10.65	(3.35)	5.44	11.04	(3.35)	6.96	(2.67)	4.09	(2.02)	1.70	(1.06)	0.95
A8	800008 [S3] †	21:53:23.78	(0.1)	+17:39:29.8	(0.1)	18.47	(4.40)	9.04	19.74	(4.52)	18.92	(4.40)	<2.04	–	>9.27	–	1.13
	800009 [S3]	21:53:23.82	(0.1)	+17:39:29.8	(0.2)	15.85	(4.06)	7.97	23.25	(4.87)	19.21	(4.42)	<4.08	–	>4.71	–	0.86
A9	800008 [S1] †	21:53:23.81	(0.5)	+17:30:21.5	(0.4)	29.62	(6.42)	9.95	40.96	(6.76)	36.34	(6.25)	<5.18	–	>7.02	–	0.62
A10	800008 [S3]	–	–	–	–	–	–	–	6.53	(3.19)	<5.62	–	<3.02	–	–	–	–
	800009 [S3]	21:53:25.26	(0.3)	+17:43:21.9	(0.2)	11.63	(3.78)	5.30	13.04	(3.79)	13.44	(3.79)	<0.43	–	>31.26	–	1.45
A11	800008 [S2]	21:53:26.40	(0.6)	+17:35:16.8	(0.3)	13.00	(3.88)	6.01	16.54	(4.16)	14.53	(3.87)	<2.98	–	>4.88	–	1.14
A12	800009 [S4]	21:53:29.01	(0.5)	+17:48:54.3	(0.6)	12.02	(4.63)	5.02	18.21	(4.65)	12.28	(3.79)	6.04	(2.69)	2.03	(1.10)	1.13
A13	800009 [S3]	21:53:31.60	(0.3)	+17:47:04.0	(0.3)	18.45	(4.51)	8.41	21.61	(4.75)	18.78	(4.39)	<3.62	–	>5.9	–	0.91
A14	800008 [S2]	–	–	–	–	–	–	–	<3.12	–	<0.40	–	<3.14	–	–	–	–
	800009 [S2]	21:53:32.82	(0.5)	+17:32:22.8	(0.8)	11.24	(4.04)	4.90	15.81	(4.34)	10.97	(3.54)	<4.98	–	>2.20	–	0.83
A15[1]	800008 [S3]	21:53:33.19	(0.1)	+17:42:10.0	(0.1)	35.17	(6.93)	11.30	36.60	(6.83)	20.15	(5.24)	16.47	(4.38)	1.22	(0.46)	1.76
	800009 [S3]	21:53:33.18	(0.1)	+17:42:09.9	(0.1)	35.34	(6.93)	11.38	40.51	(7.03)	23.19	(5.42)	17.33	(4.49)	1.34	(0.47)	2.04
A16	800008 [S2]	21:53:33.57	(0.1)	+17:37:34.7	(0.1)	31.82	(5.72)	15.44	31.59	(5.72)	23.79	(4.95)	7.77	(2.87)	3.06	(1.30)	1.22
	800009 [S2]	21:53:33.62	(0.1)	+17:37:35.2	(0.2)	28.13	(5.37)	13.84	27.33	(5.28)	21.34	(4.64)	5.93	(2.50)	3.60	(1.71)	1.00
A17[2]	800008 [S3] *	21:53:33.79	(0.1)	+17:41:15.1	(0.1)	12.59	(4.24)	5.35	15.61	(4.26)	15.15	(4.13)	<2.02	–	>7.49	–	1.65
	800009 [S3]	21:53:33.71	(0.1)	+17:41:15.3	(0.1)	15.88	(4.90)	6.24	23.77	(5.31)	19.89	(4.81)	<4.50	–	>4.42	–	2.34
A18[3]	800008 [S3]	21:53:33.98	(0.1)	+17:42:41.3	(0.1)	68.73	(9.02)	20.50	71.96	(9.05)	24.52	(5.61)	47.52	(7.11)	0.52	(0.14)	1.43
	800009 [S3]	21:53:33.95	(0.1)	+17:42:41.2	(0.1)	71.68	(9.01)	22.84	76.51	(9.14)	29.69	(5.86)	46.88	(7.02)	0.63	(0.16)	1.41
A19	800008 [S2]	21:53:34.78	(0.1)	+17:36:30.5	(0.1)	113.97	(10.77)	49.44	115.39	(10.77)	79.65	(8.95)	35.61	(5.99)	2.24	(0.45)	1.22
	800009 [S2]	21:53:34.84	(0.1)	+17:36:30.8	(0.1)	123.53	(11.25)	49.88	127.53	(11.35)	95.34	(9.81)	31.80	(5.67)	3.00	(0.62)	1.35
A20	800008 [S3]	21:53:40.77	(0.1)	+17:44:15.4	(0.1)	149.74	(12.44)	54.56	153.88	(12.48)	61.98	(7.95)	92.49	(9.65)	0.67	(0.11)	1.27
	800009 [S3]	21:53:40.76	(0.1)	+17:44:15.6	(0.1)	136.48	(11.82)	54.39	139.67	(11.87)	61.97	(7.91)	78.06	(8.86)	0.79	(0.14)	1.51
A21	800008 [S3]	–	–	–	–	–	–	–	10.34	(3.58)	6.06	(2.73)	<4.64	–	>1.31	–	–
	800009 [S3]	21:53:40.93	(0.4)	+17:45:21.1	(0.4)	7.98	(3.54)	3.74	10.81	(3.70)	9.56	(3.40)	<2.92	–	>3.27	–	1.02
A22	800008 [S1] †	21:53:43.78	(0.7)	+17:29:10.6	(0.9)	38.81	(8.15)	10.93	59.23	(8.55)	52.66	(7.62)	<8.00	–	>6.58	–	1.07
A23	800008 [S3] *	21:53:44.47	(0.8)	+17:42:58.4	(0.4)	4.87	(4.98)	3.47	13.26	(4.81)	9.48	(4.10)	3.78	(2.52)	2.51	(1.99)	4.27
	800009 [S3]	–	–	–	–	–	–	–	<7.95	–	<6.8	–	<4.12	–	–	–	–
A24	800008 [S3]	21:53:45.55	(0.2)	+17:41:47.7	(0.1)	29.40	(6.49)	9.75	31.59	(6.37)	13.61	(4.45)	19.14	(4.67)	0.71	(0.29)	2.46
	800009 [S3]	21:53:45.54	(0.1)	+17:41:47.3	(0.1)	14.77	(4.16)	6.61	15.65	(4.18)	8.18	(3.04)	7.49	(2.87)	1.09	(0.58)	1.19
A25	800009 [S3]	21:53:46.31	(0.3)	+17:46:26.6	(0.3)	45.03	(7.26)	15.54	49.25	(7.19)	44.83	(6.79)	<4.70	–	>9.54	–	1.58
A26	800008 [S2] †	21:53:47.98	(0.3)	+17:37:56.2	(0.4)	13.57	(3.83)	6.58	13.42	(3.84)	11.83	(3.54)	<2.08	–	>5.69	–	1.67
	800009 [S2]	21:53:47.96	(0.1)	+17:37:55.6	(0.2)	34.66	(5.98)	16.40	36.12	(6.07)	29.85	(5.51)	6.14	(2.53)	4.86	(2.19)	0.98
A27	800008 [S3]	21:53:47.97	(0.2)	+17:42:47.6	(0.2)	23.45	(5.01)	10.80	23.08	(4.91)	15.94	(4.09)	7.17	(2.71)	2.23	(1.02)	1.08

Table 1 – *continued*

Name	Seq. No. [Chip]	RA_X (J2000)	$\Delta\alpha_X$ ($''$)	DEC_X (J2000)	$\Delta\delta_X$ ($''$)	WAV (cts)	(err)	Sig	0.5–7 keV (cts)	(err)	0.5–2 keV (cts)	(err)	2–7 keV (cts)	(err)	S/H	(err)	PSF ratio
	800009 [S3]	21:53:47.97	(0.1)	+17:42:47.2	(0.1)	35.29	(6.02)	17.05	52.96	(7.34)	45.83	(6.82)	7.10	(2.70)	6.45	(2.63)	0.90
A28	800008 [S3]	21:53:48.84	(0.1)	+17:41:59.8	(0.2)	31.27	(5.78)	13.78	30.67	(5.70)	24.96	(5.11)	5.70	(2.52)	4.38	(2.13)	1.01
	800009 [S3]	21:53:48.85	(0.2)	+17:41:60.2	(0.2)	13.28	(4.07)	5.86	14.06	(4.08)	10.79	(3.53)	<4.10	–	>2.63	–	1.66
A29	800008 [S3]	21:53:52.85	(0.4)	+17:44:02.2	(0.3)	11.24	(3.59)	5.35	11.67	(3.60)	8.01	(2.93)	<4.20	–	>1.91	–	0.95
A30	800008 [S3]	21:53:53.61	(0.5)	+17:44:02.4	(0.7)	10.51	(3.75)	4.75	11.40	(3.76)	<4.66	–	7.36	(2.97)	<1.06	–	1.51
A31	800008 [S3]	21:53:55.00	(0.2)	+17:43:59.2	(0.6)	10.03	(3.46)	4.76	11.81	(3.62)	10.28	(3.29)	<3.02	–	>3.40	–	0.96

The exposure times are 9.83 ks for 800008 and 9.13 ks for 800009.
The counts given by the WAVDETECT algorithm (columns 7 and 8) are for the total 0.5–7 keV band, and differ from the counts given in columns 10 and 11 due to the different background estimation methods (see text for details).
The significance given in column 9 is that obtained from WAVDETECT.
S/H is the ratio of the counts in the 0.5–2 keV band (columns 12 and 13) and those in the 2–7 keV band (columns 14 and 15).
The PSF ratio given in the final column is the ratio of the source size to the PSF size at the source location, as output from the WAVDETECT algorithm.
Sources marked with a * may have their counts in the soft band (and hence the S/H ratio) affected by the proximity to the cluster.
Sources marked with a † are close to the edge of the chip, where dither may affect the counts and S/H ratios.
[1]This source is CXOU J215333.2+174209 (source 2) in Fabian et al. (2000), source 3 (updated to CXOU J215333.2+174211), in Cowie et al. (2001), and source B in Wilman, Fabian & Gandhi (2000a).
[2]This source is CXOU J215333.8+174113 (source 3) in Fabian et al. (2000), and source 2 (updated to CXOU J215333.8+174116) in Cowie et al. (2001).
[3]This source is CXOU J215334.0+174240 (source 1) in Fabian et al. (2000), source A in Wilman et al. (2000), and source 1 (updated to CXOU J215334.0+174242) in Cowie et al. (2001).

the AGN itself undetectable at optical and near-infrared (NIR) wavelengths. Obscured AGN plausibly explain the spectral shape of the XRB (Setti & Woltjer 1989; Madau, Ghisellini & Fabian 1994; Comastri et al. 1995).

Here we report on the field of the cluster A 2390 (Fabian et al. 2000; Allen, Ettori & Fabian 2001; Cowie et al. 2001), where we detect 31 serendipitous sources in two separate *Chandra* observations totalling about 19 ks. Two have stellar optical spectra, and of the remaining 22 optical identifications we have measured spectroscopic redshifts for 13 and obtain photometric redshifts from optical and NIR images of a further four. We test the photometric redshift approach for such sources against the spectroscopic results where both are available. The resulting redshift distribution stretches out to $z \sim 3$, with a peak between $z = 1$–2. Ten of our sources have hard X-ray spectra indicating a spectral slope flatter than that of a typical unabsorbed quasar. X-ray spectral fitting has been carried out on the eight brightest sources. Some X-ray variability is detected between the two observations.

Strong gravitational lensing has enhanced three sources. These were also detected in the mid-IR by ISOCAM on the *Infrared Space Observatory* (*ISO*) in a very deep exposure of A 2390 (Altieri et al. 1999). Two of these appear to be genuine obscured quasars.

2 OBSERVATIONS AND RESULTS

2.1 Detection of the X-ray serendipitous sources

The $z = 0.228$ cluster A 2390 was observed on two occasions with the *Chandra* X-ray observatory: on 2000 October 08 (with sequence number 800008 and a focal plane temperature of −120C) for 9.83 ks; and on 1999 November 05 (seq. no. 800009 and a focal plane temperature of −110C) for 9.13 ks. The analysis of the X-ray emission from A 2390 itself is published elsewhere (Allen et al. 2001); here we investigate the properties of the serendipitous point sources identified in the field. For each observation, the cluster was placed ∼1 arcmin from the centre of chip ACIS-S3, and five of the chips (ACIS-23678) were operating. The roll angle differed only slightly between the two observations (−171° for 800008, −190° for 800009), so there is a large overlap between their fields of view.The 800009 data set was updated for the correct gainfile (as of 2000 October). The light curve of the S3 data showed no evidence for flaring of the background level during either observation, so we use the data from the full duration of each exposure. The data were exposure-map-corrected to account for the decrease in effective area off-axis.

We searched the total *Chandra* field of view for serendipitous sources using the Chandra Interactive Analysis of Observations (CIAO) WAVDETECT detection algorithm. WAVDETECT was run on the data from each chip in the 0.5–7 keV band, with the data at three binnings: the original unbinned pixels (each of 0.5 arcsec), and binned by two and four pixels (i.e., 1- and 2-arcsec bins respectively). We find that this is an efficient way of detecting the widest range of sources, as the best precision can be obtained for most sources from the unbinned image, but the fainter or more diffuse sources [especially in chips where the point spread function (PSF) is more extended] appear significant only at higher binnings. We experimented with a full range of wavelet scales (using the $\sqrt{2}$ sequence of 1, 1.414, 2.0 … 16.0 pixels) to pick up different-sized sources, and set the significance threshold for sources at 10^{-5} for the four-pixel binning, and at 10^{-6} for the two-pixel binning and unbinned data.

We discarded all sources with fewer (non-background-subtracted) than 10 counts as too marginal, and any found within 20 arcsec of the edge of each chip. The spacecraft dither is on this scale, and so there is a danger that some of the counts for sources too near the chip edge will be lost during the observation. Each source was examined by eye, in order to discard any that could be due to the prominent stripes apparent in the background of some of the chips. These stripes appear at soft energies, and are most noticeable in chip ACIS-S4; we include only one (totally unambiguous) source from this chip (A12). Other chips marginally affected by background stripes are chips I2, I3 and S2 in the 800009 observation. We conclude with a sample of 31 serendipitous sources, and list their X-ray properties in Table 1. The first observation (800009) occurred when the registration between the *Chandra* coordinates and the real sky was incorrect. We have re-registered the data set using the 12 sources that were detected in common between the two separate observations. All the coordinates given for the 800009 data set in Table 1 have been corrected for this $\sim$2-arcsec offset.

We also estimated the counts in each source in three energy bands: 0.5–2 keV (soft), 2–7 keV (hard) and 0.5–7 keV (total). The counts were taken from a box centred on a source, with a length given by the square root of the number of pixels in the source cell (as given from WAVDETECT). The local background was estimated from a concentric box with a length 5 times longer. The background box was offset if it would otherwise spill over the edge of the chip, or would include a close neighbouring source. Where the source counts (in any band) were less than twice the error on that value, we replaced the value with an upper limit set at twice the error. For nearly all the sources the counts obtained from WAVDETECT and our box statistics agree within the errors. The only major exceptions are sources A1 – the most off-axis, and a very diffuse source – and A22, which is rather close to the edge of the chip. We used the background-subtracted counts in the hard and soft bands to estimate a soft-to-hard ratio (S/H) for each source. The higher sensitivity of *Chandra* below 2 keV means that even genuinely hard sources can still show plenty of counts in our soft band (see, e.g., Crawford et al. 2002). The WAVDETECT results, counts for each source in the different bands, and the S/H ratios are presented in Table 1. A few of the sources also varied significantly in brightness over the 11 months between the two observations. Specifically, sources A2 and A23 brightened over this period, whilst A3, A4, A6, A14, A26 and A27 all faded (Fig. 1). The colours of A6 and A27 also appeared to soften appreciably over this period.

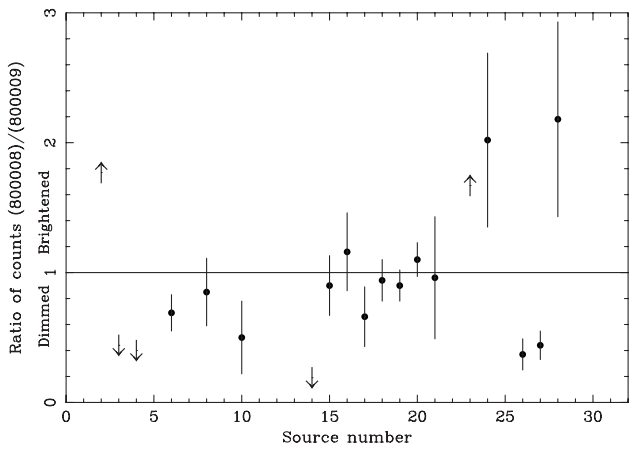

Figure 1. The ratio of counts in the serendipitous sources in common between 800009 (earlier) and the 800008 (later) observations. 1σ errors are shown on the ratios.

Our faintest sources typically have 10–11 counts over the full 0.5–7 keV energy range; 10 counts corresponds to countrates of 1.017×10^{-3} ct s^{-1} in the 800008 observation and 1.095×10^{-3} ct s^{-1} for the 800009 observation. We use PIMMS to translate source counts into observed fluxes, assuming a power-law model with slope $\Gamma = 1.4$ that is absorbed only by the Galactic column density in this direction ($\sim 6.81 \times 10^{20}$ cm^{-2}; Stark et al. 1992). A source with a countrate of 10^{-3} ct s^{-1} is predicted to have a (0.5–7 keV) flux of 6.7×10^{-15} erg cm^{-2} s^{-1} if observed in a back-illuminated (BI) chip (S1 or S3), or 1.1×10^{-14} erg cm^{-2} s^{-1} if observed in a front-illuminated (FI) chip. These fluxes decrease to 4.3×10^{-15} and 8.2×10^{-15} erg cm^{-2} s^{-1} (for BI- and FI-chips respectively) if a steeper slope of $\Gamma = 2$ is assumed, or increase to 1.5×10^{-14} and 1.3×10^{-14} erg cm^{-2} s^{-1} if there is an excess absorption of $\sim 10^{22}$ cm^{-2}.

2.2 Infrared and optical photometry

We reduced optical images of the field around A 2390 available from the archives of the Isaac Newton Group telescopes, and the Canada-France-Hawaii Telescope (CFHT). Where the position of a serendipitous source was not covered in the field of view of one of the archival data sets, we examined the Digitized Sky Survey (DSS; second generation) images. *J*-, *H*- and *K*-band images of 12 of the serendipitous sources from the 800009 observation were obtained on the nights of 2000 August 10 and 11 at the United Kingdom Infrared Telescope (UKIRT), using the UFTI full-array with a 92-arcsec field of view. A summary of the observations (archival and dedicated) taken is shown in Table 2. The optical data were flux-calibrated using standard Landolt stars, except for the CFHT *I*-band data, which was cross-calibrated against the flux-calibrated WHT *I*-band image. The flux standards for the NIR data were taken from the UKIRT faint-star catalogue.

Magnitudes of the sources were obtained by using PHOT in IRAF, taking a consistent aperture in all the bands in order to provide accurate colours for later use in photometric redshift fitting. The optical and NIR magnitudes are listed in Table 3. The seeing for the

Table 2. A 2390 observations.

Band	Date	Telescope & Instrument	Plate Scale (arcsec pixel^{-1})	Filters	Seeing (arcsec)	Typical Exposure (seconds)
B	1994 Dec 08	WHT Prime Focus	0.421	Kitt Peak 1	3.8	500
R	1994 Jun 06	INT Prime Focus	0.590	Kitt Peak 3	1.6	600
I	1994 Dec 08	WHT Prime Focus	0.421	Kitt Peak 1	1.4	300
I	1990 Oct 16	CFHT focam	0.205	CFHT #1809	0.7	700
J, *H*, *K*	2000 Aug 10/11	UKIRT UFTI	0.091	J98, H98, K98	0.6	540

Table 3. A 2390 photometry (Vega magnitudes).

Object	RA_{opt} (J2000)	Dec_{opt} (J2000)	*B*	*R*	*I*	*J*	*H*	*K*	Aperture diameter (arcsec)
A3	21:52:55.80	17:44:34.1	$>22.5^{D}$	$>21.0^{D}$	–	–	–	–	
A4	21:53:00.95	17:44:52.4	22.0 ± 0.5^{D}	$>21.0^{D}$	–	–	–	–	
A5	21:53:04.92	17:38:33.8	16.89^{A}	14.80^{A}	–	–	–	–	
A6	21:53:20.72	17:41:19.6	$>22.5^{D}$	21.96 ± 0.10	–	–	–	–	4.5
A7	–	–	$>22.5^{D}$	>23.40	>22.25	–	–	–	4.5
A8	21:53:23.86	17:39:30.3	23.69 ± 0.37	21.84 ± 0.08	20.24 ± 0.06	19.50 ± 0.06	18.38 ± 0.04	17.42 ± 0.03	4.5
$A9^{A}$	21:53:23.68	17:30:19.9	13.31^{A}	12.05^{A}	–	–	–	–	–
A10	21:53:25.30	17:43:22.3	22.39 ± 0.09	19.91 ± 0.03	19.01 ± 0.03	–	–	–	4.5
$A11^{D}$	21:53:26.47	17:35:17.4	22.0 ± 0.5^{D}	$>21.0^{D}$	–	–	–	–	
$A12^{P}$	21:53:29.05	17:48:54.7	$>22.5^{D}$	$>21.0^{D}$	–	19.48 ± 0.05	18.35 ± 0.03	17.70 ± 0.03	4.5
A13	21:53:31.64	17:47:04.4	$>22.5^{D}$	$>21.0^{D}$	–	–	–	–	
A14	21:53:32.86	17:32:23.8	$>22.5^{D}$	$>21.0^{D}$	–	18.32 ± 0.03	17.59 ± 0.03	16.78 ± 0.02	4.5
$A15^{S}$	21:53:33.22	17:42:10.4	>23.72	>23.25	>22.88‡	>21.71	20.07 ± 0.06	18.83 ± 0.04	4.5
A16	21:53:33.65	17:37:35.6	22.0 ± 0.5^{D}	20.98 ± 0.06	–	19.82 ± 0.07	19.55 ± 0.10	18.90 ± 0.10	2.7
A17	21:53:33.75	17:41:15.8	>23.66	22.99 ± 0.24	21.11 ± 0.10‡	19.38 ± 0.03	18.59 ± 0.03	17.58 ± 0.02	2.7
A18	21:53:33.99	17:42:41.6	>23.74	23.86 ± 0.37	21.13 ± 0.11‡	18.65 ± 0.03	17.57 ± 0.02	16.49 ± 0.02	4.5
A19	21:53:34.88	17:36:31.7	20.50 ± 0.30^{A}	19.35 ± 0.03	–	18.74 ± 0.03	17.80 ± 0.03	17.37 ± 0.03	4.5
A20	21:53:40.80	17:44:16.0	21.90 ± 0.07	20.18 ± 0.03	19.38 ± 0.02	18.22 ± 0.02	17.64 ± 0.02	16.43 ± 0.02	4.5
A21	21:53:40.97	17:45:21.6	$>22.5^{D}$	>23.34	–	–	–	–	4.5
$A22^{D}$	21:53:43.87	17:29:12.3	20.48^{A}	20.5 ± 0.5^{D}	–	–	–	–	
A23	–	–	>23.67	>23.89	>22.49	–	–	–	2.7
A24	21:53:45.58	17:41:47.8	20.26 ± 0.04	18.24 ± 0.02	17.41 ± 0.03	16.31 ± 0.02	15.63 ± 0.02	14.90 ± 0.02	4.5
A25	21:53:46.35	17:46:27.0	20.20^{A}	17.76^{A}	–	–	–	–	
A26	21:53:48.00	17:37:56.1	20.10^{A}	19.85 ± 0.03	–	–	–	–	4.5
A27	21:53:47.98	17:42:48.0	21.97 ± 0.09	20.91 ± 0.05	19.22 ± 0.04	18.97 ± 0.04	18.42 ± 0.04	17.62 ± 0.03	2.7
A28	21:53:48.87	17:42:00.0	22.20 ± 0.10	21.30 ± 0.08	20.58 ± 0.05	18.98 ± 0.03	18.19 ± 0.03	17.21 ± 0.02	4.5

The following sources are not included in the table as they are not in the field of view of the archival optical data sets, and there is no obvious identification in either the DSS *B* or *R* images: A1 A2, A29, A30 and A31.

The RA_{opt} and Dec_{opt} listed in columns 2 and 3 are from the *R*-band image of Cowie et al. (2001), except for those sources whose name is marked by ^{A} or ^{D} where the position is from the APM or DSS data respectively.

In columns 4 and 5, a magnitude (or upper limit) marked by a ^{D} or ^{A} was estimated from the DSS (second-generation) image, or from the Palomar Observatory Sky Survey as scanned from the APM at Cambridge, as the source was not in the field of view of the archival optical data. The remaining magnitudes are either from the INT (*R*-band), or the WHT (*I*- and *B*-band) image, except for the three *I*-band magnitudes marked ‡, which were measured from the deeper CFHT image.

The source marked ^{P} has a systematic photometric uncertainty of 14 per cent in *J*, 12 per cent in *H* and 8 per cent in *K*. The value stated has been calibrated against all standards observed through the night – see text.

The aperture size stated in the last column is for the infrared data. For the optical data, the seeing-corrected apertures were typically larger.

The source marked ^{S} also has *ISO* 6.75- and 15-μm detections of 110 and 350 μJy respectively (Lémonon et al. 1998). These translate to magnitudes of 14.8 and 11.9.

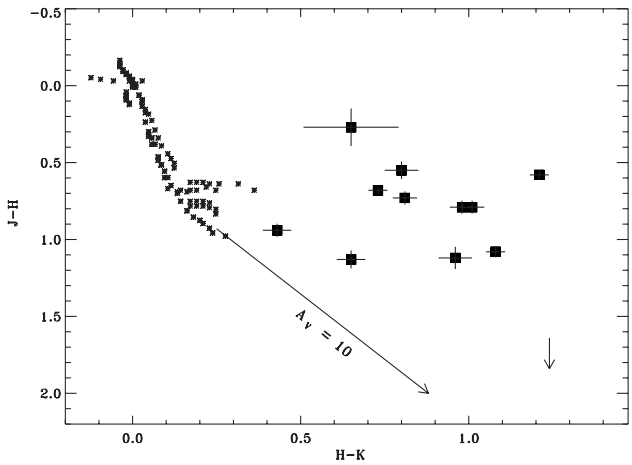

Figure 2. The near-infrared colour–colour plot for the A 2390 background sources (filled squares), shown with 1σ error bars. The star symbols show the infrared colours of main sequence, giant and supergiant stars of all spectral types (O–M). The upper limit is that of A15, which has a particularly large $J-H$ break.

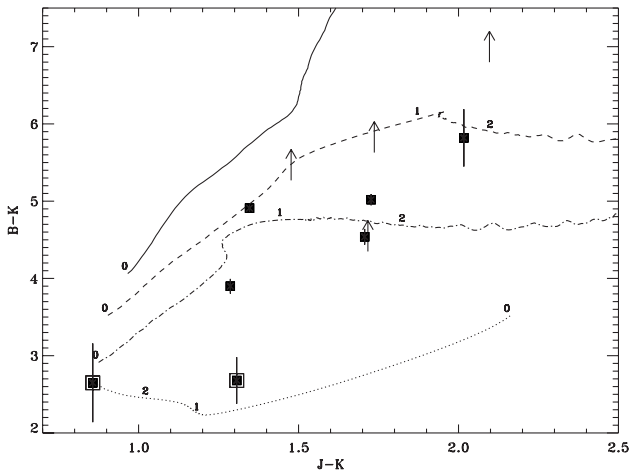

Figure 3. The optical–NIR colours of the A 2390 background sources (filled squares and arrows), again shown with 1σ error bars. The two sources outlined by a larger open square are A16 and A19. We do not include the source A15 because it is a lower limit on both axes. All colours have been corrected for Galactic reddening. The lines show the predicted colour tracks for CWW E (solid), Sbc (dashed) and Scd (dot-dashed) models (see text), while the dotted line is a colour track for a median radio-quiet QSO template from Elvis et al. (1994). The numbers associated with each line mark the redshift of the template at that point.

B band was very large; a typical aperture of 4.5-arcsec diameter was chosen for most objects, except for some of the very faint ones and for objects with close neighbours; for these we used an aperture of 2.7-arcsec diameter, and seeing corrections were made in all the bands. Since this is a crowded field, a very large sky aperture was used estimate the background in the optical data, relying on PHOT K-sigma clipping to remove any sources in the background box. A limiting magnitude was estimated for each source as three standard deviations of the sky flux, multiplied by the square root of the number of good pixels in the object aperture. The NIR images were typically uncrowded, and background estimation could be performed with apertures that did not include other sources. The magnitudes for our sources agree well with the magnitudes obtained by Cowie et al. (2001) when account is taken of the fact that the apertures we use are large (typically a diameter of 4.5 arcsec to encompass the poor PSF in the optical) as compared to the 2-arcsec diameter used in Cowie et al.

An NIR colour–colour plot (Fig. 2) demonstrates that the sources we imaged are not stars. Even the source closest to the stellar locus (A19) is a found to be a quasar, not a star, from the optical spectrum (see next section). An optical–NIR colour plot of the same sources and a median QSO template (Elvis et al. 1994) is shown in Fig. 3. The QSO template was constructed using UV-bright ('UVSX') radio-quiet QSOs with median redshift of ≈ 0.15. The template thus represents local bright X-ray QSOs (and their *k*-correction with redshift) with little obscuration to their UV light. Only two of our sources have colours clearly resembling the unobscured QSO population. These two sources are A16 and A19, both of which are obvious quasars from their optical spectra. The rest of the sources show red $B-K$ colours which are closer to those predicted for Coleman, Wu & Weedman (1980) galaxy templates (shown without reddening) with *k*-corrections only ($z=0$ at the blue end, going up to $z\approx 2.5$ for the Sbc and Scd models at the red end).

Whereas AGN line intensity contribution dominates the broad-band flux in only one source (A20, discussed later), any contribution from an AGN continuum is difficult to quantify. This is especially true of the soft X-ray sources. For instance, A28, with an X-ray S/H ratio as high as 4.4 and a strong Mg II λ2798 emission line (Section 2.3), is possibly an unobscured QSO. The broad-band optical–NIR colours, however, do not easily tally with this (a quasar template which fits the *B*-band flux underpredicts the NIR light by a factor of at least 10). It may be the case that while the blue light is QSO dominant (consistent with the large Mg II equivalent-width), the NIR light has a large contribution from a red host. In fact, a composite template with a monochromatic flux ratio of 30 between a QSO (Francis et al. 1991) and an elliptical galaxy (Coleman et al. 1980) at 2798 Å can fit the photometric data at $z\approx 1$ moderately well, though not as successfully as the S0 template fitted by HYPERZ (Section 2.4).

2.3 Optical spectroscopy

We took optical spectra of 15 of the serendipitous background sources listed in Table 1; the selection of which sources to observe was random, with a preference only for those with definite optical identifications, and which were least off-axis in the *Chandra* observations. The spectra were taken on 2000 September 28 and 29 with the Keck Echellette Spectrograph and Imager (ESI) (Epps & Miller 1998), used in low-resolution mode with a 1-arcsec slit. The nights were photometric, with seeing of about 0.7 arcsec. Targets were observed at three positions along the slit with 600-s exposure times at each position, and the median of the observations was used to form the sky. The observations were then sky-subtracted and aligned before the spectrum was extracted. The wavelength calibration was determined from the night-sky emission lines. The final spectral resolution is 17 Å, and the data cover the 5000–10 000 Å wavelength range. Redshifts were then measured by hand for each object, using a standard set of emission and absorption lines for galaxies and AGN. The spectra were not flux-calibrated.

11 of the sources show clear emission-line spectra (Fig. 4), with redshifts ranging from 0.214 to 1.675 (Table 5). The equivalent widths of the principal emission lines are tabulated in Table 4, as well as the velocity width of the Mg II λ2798 emission line (where it is present). Six or seven of the sources (A4, A13, A16, A19, A26,

Table 4. Equivalent widths of emission lines, in Å.

Source	C III]λ1909	Mg II λ2798	FWHM of Mg II (km s^{-1})	[O II]λ3727	Hβ	[O III]λ5007	Hα	[N II]λ6584	[S II]λ6731
A4	–	21.2 ± 1.0	4202 ± 226	$1.7^{+1.2}_{-1.1}$	–	–	–	–	–
A6	–	$35.6^{+2.3}_{-2.2}$	6995 ± 465	$9.1^{+1.5}_{-1.4}$	–	–	–	–	–
A8	–	<2.5	–	24.8 ± 0.7	$15.2^{+1.1}_{-1.2}$	27.9 ± 2.0	–	–	–
A10	–	–	–	–	–	–	0.9 ± 0.5	$5.4^{+0.6}_{-0.5}$	–
A13	$33.6^{+1.8}_{-1.7}$	$49.6^{+2.4}_{-2.3}$	8455 ± 139	–	–	–	–	–	–
A16	$25.2^{+2.2}_{-2.0}$	$33.9^{+2.5}_{-2.4}$	8203 ± 453†	–	–	–	–	–	–
A18	–	–	–	$13.5^{+3.1}_{-2.7}$	–	–	–	–	–
A19	30.7 ± 1.4	45.6 ± 1.9	8271 ± 403†	–	–	–	–	–	–
A20	–	–	–	163.6 ± 6.1	$71.1^{+7.2}_{-7.3}$	$711.8^{+26.1}_{-25.7}$	$249.3^{+11.7}_{-11.3}$	$53.5^{+6.5}_{-6.6}$	10.7 ± 6.2
A24	–	–	–	–	–	35.1 ± 1.6	$18.7^{+1.0}_{-0.9}$	$32.2^{+1.5}_{-1.0}$	2.7 ± 0.8
A26	24.2 ± 1.2	23.0 ± 0.7	3825 ± 126	–	–	–	–	–	–
A28	–	79.2 ± 3.7	6089 ± 277	–	–	–	–	–	–

†A single Gaussian is not a particularly good fit to the Mg II line in A16 and A19, suggesting that the equivalent width and velocity width are greater than tabulated.

Table 5. A 2390 redshifts.

Source	$z_{\rm spectroscopic}$	$z_{\rm photometric}$ (90% confidence)	Reduced χ^2 (d.o.f.)	Galaxy Type	Age (Gyr)	A_V	M_B	$z_{\rm secondary}$
A4	1.2172	–	–	–	–	–	–	
A6	1.0690	–	–	–	–	–	–	
A8	0.8030	0.79 (0.75,0.82)	1.98 (5)	Burst	0.36	0.60	−22.44	4.33
A10	0.2242	–	–	–	–	–	–	
A12^{P}	–	2.28 (1.67,3.33)	0.04 (4)	Burst	0.26	0.30	−24.98	0.63
A13	1.5933	–	–	–	–	–	–	
A14	–	1.35 (0.89,1.80)	0.04 (4)	Burst	0.72	0.00	−24.47	5.29
A15	–^{C3}	2.78 (2.07,3.34)	0.19 (6)	E	1.43	1.80	−21.44‡	3.16
A16	1.6321	1.35 (1.17,2.06)	1.08 (4)	QSO	–	0.30	−23.25	0.36
A17	1.466^{C2}	1.11 (0.99,1.15)	0.39 (5)	Burst	0.51	0.60	−21.77‡	4.63
A18	1.467^{C1}	1.45 (1.31,1.53)	2.02 (5)	Burst	2.60	0.00	−23.20‡	5.72
A19	1.6750	0.32 (0.22,0.42)	3.65 (4)	QSO	–	0.60	−21.66	0.90
A20	0.305	0.22 (0.18,0.38)	1.40 (5)	CWW Scd with AGN	2.60†	0.60	−19.57	0.33
A24*	0.214	0.26 (0.15,0.52)	0.42 (5)	E	4.5	0.00	−22.02	0.47
A26	1.5187	–	–	–	–	–	–	
A27	–	0.87 (0.82,0.92)	5.15 (5)	Burst	0.18	0.00	−23.62	0.54
A28	1.0330	1.21 (1.15,1.33)	0.19 (5)	S0	0.72	0.90	−23.61	1.63

M_B in column 8 is the absolute Vega magnitude in the *B* Bessell filter. Those sources with a magnitude marked by a ‡ have been corrected for the magnification due to gravitational lensing.
^{C1}This is a spectroscopic redshift from Cowie et al. (2001).
^{C2}This is a spectroscopic redshift from Cowie et al. (2001) based on the single identification of a line, but also consistent with their photometric redshift estimate of 1.5 ± 0.2. A different identification would imply a redshift of 2.317 instead.
^{C3}Cowie et al. (2001) obtain a photometric redshift of $2.6^{+0.1}_{-0.2}$.
^{P}There is a high degree of degeneracy between this redshift estimate and the secondary solution, with small changes in the photometry. See text for details.
*This source is identified as an Sbc galaxy with a redshift of $z = 0.21501$ by Yee et al. (1991). A fit to an Sbc template gives $z_{\rm phot} = 0.3$.
†This is a Coleman et al. (1980; CWW), observed, fixed-age SED. The age has been determined by associating with a Bruzual–Charlot synthetic spectrum with redshift and reddening fixed to the values stated.

A28 and maybe A6) clearly have spectra of Type-I (i.e., quasar-like) AGN, with broad Mg II lines of equivalent width greater than 20 Å. A20 and A24 resemble line-luminous Type-II AGN, and a further two sources (A5 and A25) have stellar spectra (Fig. 5). There are no significant spectral features in A15 (Fig. 6), and we detect the [O II] emission line in the spectrum of A18 at the spectroscopically confirmed redshift of $z = 1.467$ from Cowie et al. (2001). The final two sources (A8 and A10) show relatively weak narrow emission lines.

2.4 Photometric redshifts

We do not have optical spectra for all our sources, and it is clear that in the case of the fainter sources – those similar to A15 (Fig. 6) – such spectra would not necessarily help the identification or provide a redshift. We thus investigate whether photometric redshift fitting techniques can allow us to estimate redshifts for those sources with NIR magnitudes. We use HYPERZ, a publicly available code (Bolzonella, Miralles & Pelló 2000) which matches template spectra to the observed spectral energy distribution (SED). The SED is input as the observed magnitudes and their errors in as many bands as possible, and the template spectra are convolved with the filter response in each of the input bands. The filter response includes the quantum efficiency of the CCD, which is particularly important in the *I* band where the response of the CCD falls rapidly toward longer wavelengths

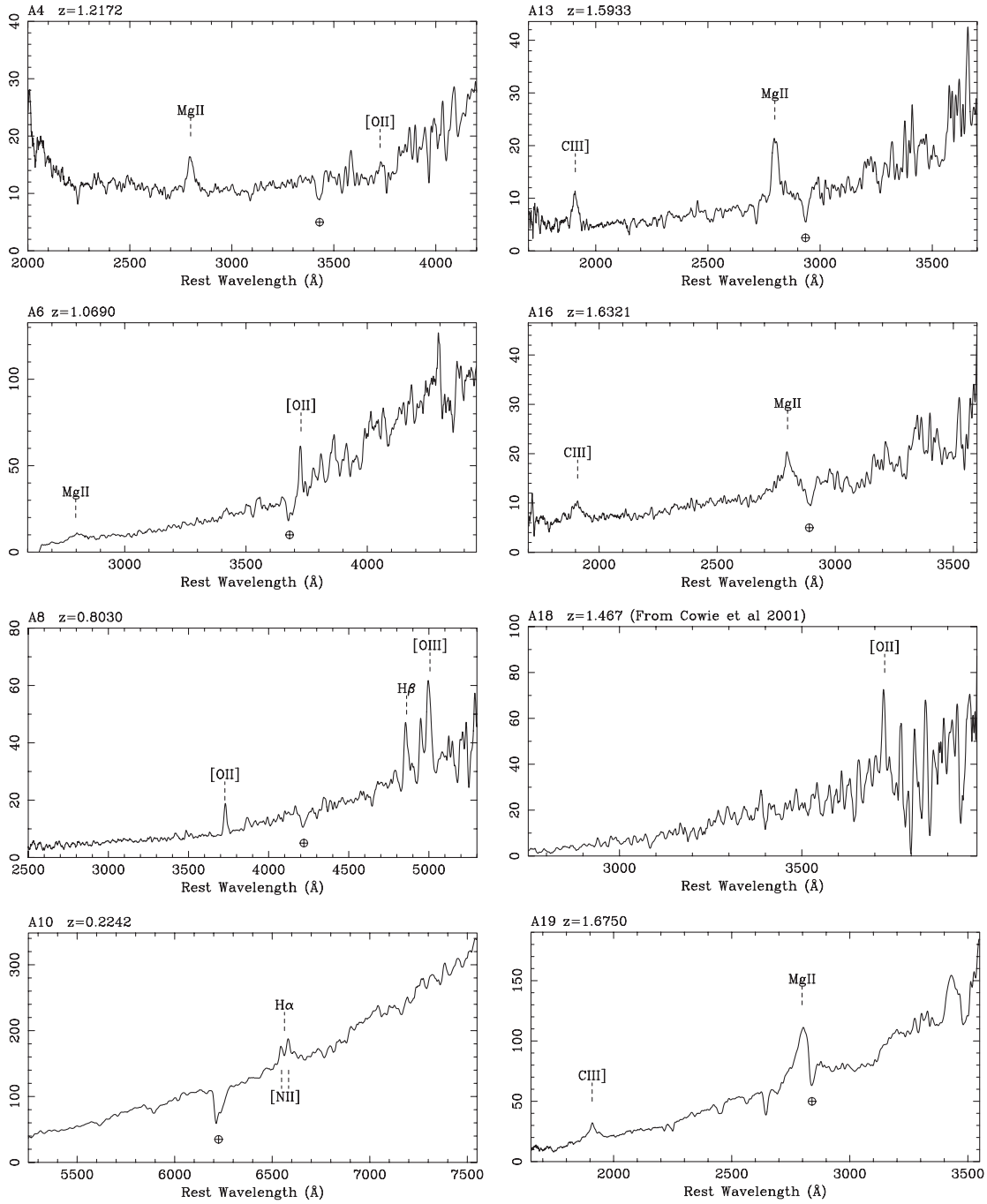

Figure 4. The Keck spectra of the serendipitous sources in the field of A 2390. The spectra are not flux-calibrated, and have been smoothed by 20 Å. The ⊕ symbol in each spectrum marks the prominent atmospheric absorption feature at around 7600 Å.

around 9000 Å. The IR filter responses were also folded with the atmospheric transmission at Mauna Kea, which is affected strongly by water vapour absorption features.

The redshift, age and internal reddening of the templates are varied in order to obtain the maximum-likelihood χ^2 solution. The template spectra chosen comprised Bruzual & Charlot (1993) synthetic spectra – with a solar metallicity and a Miller–Scalo initial mass function – and empirical SEDs observed by Coleman et al. (1980, hereafter CWW). Both sets of templates range from a single burst of star formation (SF) through ellipticals and spirals (with exponentially decaying SF rates) to a model for continuous SF in an irregular galaxy. The classification of the CWW spectra is based on the observed morphology of the objects, while the Bruzual & Charlot model galaxy type is set according to the SF time-scale.

The relatively red $B-K$ colours of all but two of our objects (Fig. 3) suggest that their light is dominated by evolved galaxy contributions or that any quasar light is obscured by several magnitudes of extinction, and photometric redshift fitting should work well for these. Standard models for the synthesis of the hard XRB (Setti & Woltjer 1989; Wilman & Fabian 1999; Wilman, Fabian & Nulsen 2000) predict some of the serendipitous sources

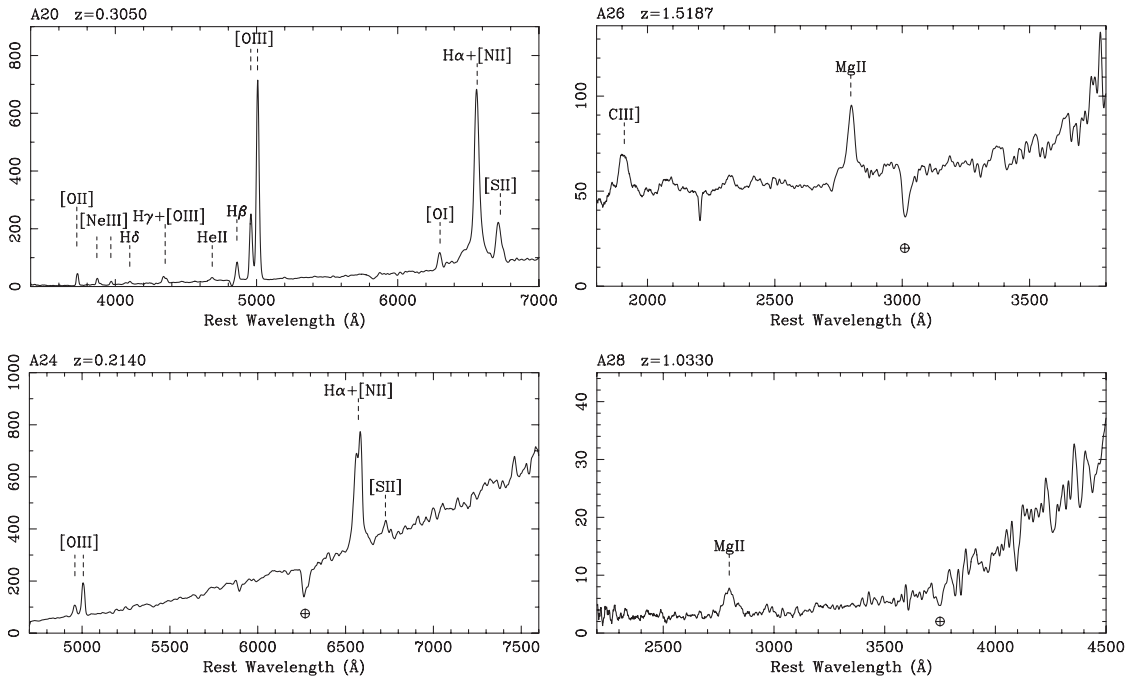

Figure 4 – *continued*

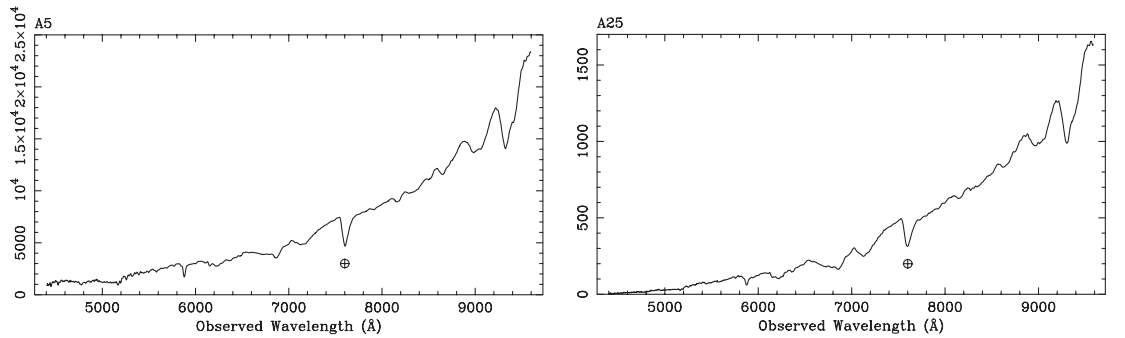

Figure 5. The Keck spectra of the two serendipitous sources in the field of A 2390 identified as stars (A5 and A25). The spectra have not been flux-calibrated or smoothed, and the ⊕ symbol in each spectrum marks the prominent atmospheric absorption feature at around 7600 Å.

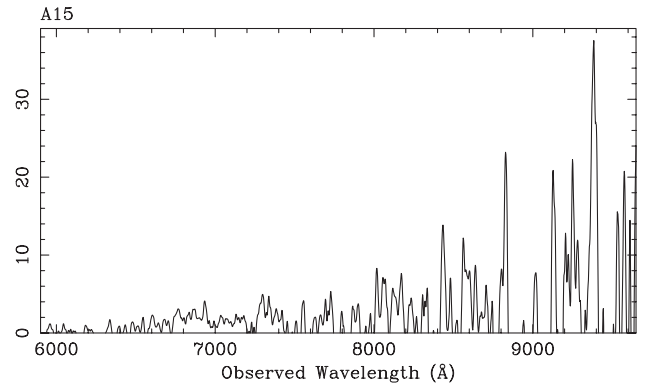

Figure 6. The Keck spectrum of the serendipitous source A15.

to be heavily obscured AGN. We thus created a set of template galaxies with such components. A standard broken power-law AGN continuum (Granato, Danese & Franceschini 1997) was assumed over the NIR/optical range and reddened with dust using the radiation transfer code DUSTY (Ivezić, Nenkova & Elitzur 1999). Since nothing is known about the dust around these sources without any (a priori) redshift information (except that the dust is probably hot at hundreds of degrees Kelvin; see Wilman, Fabian & Gandhi 2000, hereafter WFG), a number of models were constructed by varying the dust temperature, composition, optical depth and normalization of the AGN-SED to host-galaxy-SED. The reddened AGN component was added to each of the CWW spectra; one example of this is shown in Fig. 7, for the Scd CWW template. With the typical dust properties and composition found in WFG, all the optical light is assumed to be depleted and to emerge preferentially in the mid-IR regime, with some contribution in the NIR.

HYPERZ has a number of options to account for undetected objects, and we adopted the recommended procedure for medium–deep surveys such as ours, setting the flux of a non-detected object and its 1σ error equal to $F_{\rm lim}/2$ in a filter, where $F_{\rm lim}$ is the flux corresponding to the limiting magnitude in that band.

The Galactic column density of $6.81 \times 10^{20}\,{\rm cm}^{-2}$ in the direction of this cluster corresponds to a reddening $E(B-V) = 0.12$. HYPERZ dereddens the observed fluxes according to the Galactic reddening law of Allen (1976). Any reddening

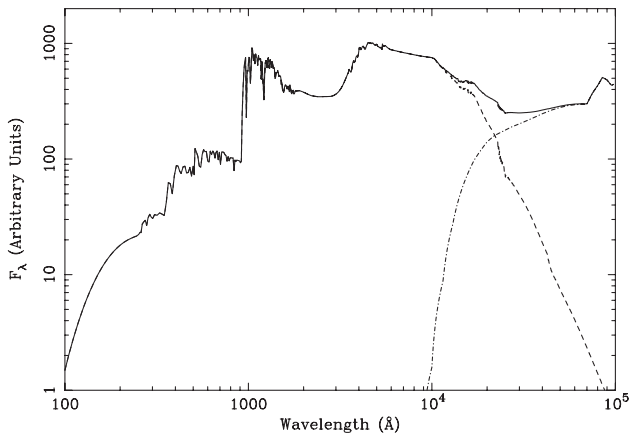

Figure 7. The combined spectrum (solid line) of the CWW Scd template (dashed) with an AGN component (dot-dashed) reddened by DUSTY and normalized to have 50 per cent of the total flux at 2.2 μm.

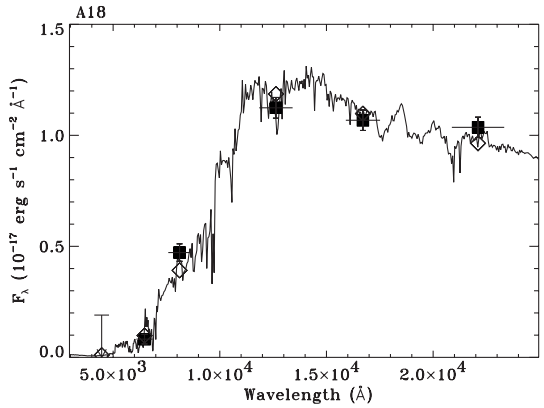

Figure 8. The best-fitting spectrum (solid line) for A18 compared to the optical and near-infrared fluxes (solid square markers and *B*-band limit). The galaxy SED is a single Bruzual & Charlot (1993) stellar burst model at $z_{\rm phot} = 1.45$, close to $z_{\rm spec} = 1.467$. The *x*-error bars are the bandwidths of the filters calculated by HYPERZ according to a Gaussian approximation, and the open diamond markers show the integrated fluxes of the template SED through the individual filters.

internal to the galaxy itself was assumed to follow the Calzetti reddening law (Calzetti et al. 2000), with a fitting range of A_V between 0.0 and 3.0, in steps of 0.3. The redshift range considered for most objects was 0.0 to 6.0 in steps of 0.05. A maximum absolute Vega magnitude of -25.0 in the *B*-band (Bessell filter) for an $H_0 = 50\,{\rm km\,s^{-1}\,Mpc^{-1}}$, $q_0 = 0.5$ cosmology was assumed. The results of the photometric-redshift-fitting procedure are shown in Table 5, with examples of the best-fitting SED for A18 shown in Fig. 8 and for A15 in Fig. 9. Given this model, Fig. 9 also shows the contours of confidence for variation of the age of the template galaxy and the amount of reddening required, demonstrating the need for reddening for a range of feasible host galaxy ages.

The photometric redshift estimate agrees well with the spectroscopic measurement (from this paper and from Cowie et al. 2001; see Table 5) for the four sources with narrow-line optical spectra (A8, A18, A20 and A24), and fairly well for one of the broad-line object A28. We emphasize that these results were not manipulated to match the spectroscopic redshifts, but constructed as a 'blind' test of the photometric redshift-fitting procedure. Our photometric redshift estimates using galaxy

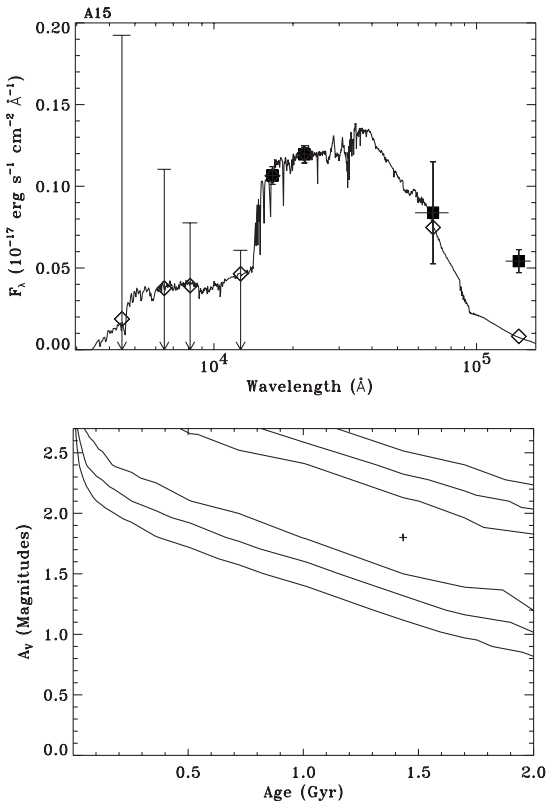

Figure 9. (Top) The most likely HYPERZ SED for A15 compared to the data, based on limits in *B*, *R*, *I* and *J* bands and detections in *H*, *K* and at 6.75 μm. The diamonds show the integrated fluxes of the template SED through the individual filters. (Bottom) Contours of confidence between the age of the elliptical host galaxy model at $z = 2.78$ and the amount of intrinsic reddening required. The cross indicates the best model, while the confidence intervals are at probabilities of 68.3 per cent ($\Delta\chi^2 = 2.3$), 95.4 per cent ($\Delta\chi^2 = 6.7$) and 99.7 per cent ($\Delta\chi^2 = 11.8$). This illustrates the need for reddening in this object, for all host galaxy ages up to 2 Gyr.

templates do not agree so well with the spectroscopic redshifts of A16 and A17, and the estimate is particularly bad for A19; in all three cases the secondary solution to the photometric redshift is no better.

We have a further three sources (A12, A14 and A27) for which we obtain a photometric redshift without spectroscopic confirmation. We note that A12 was observed during partial cirrus coverage, which leads to a systematic photometric uncertainty of about 10 per cent in flux when calibrated against the standard star observed nearest in time, as opposed to calibration against all stars observed through the night. Although this in itself is not a significant uncertainty, it creates a degeneracy in the photometric redshift estimate for this source, with the primary solution $z_{\rm phot} = 2.28$ and the secondary solution $z_{\rm phot} = 0.66$ being almost equally likely, depending on the calibration. This is because there is no *I*-band magnitude available, and we have only relatively shallow DSS limits in the *B* and *R* bands, thus reducing the constraints on this object. *I*-band photometry would be a strong constraint to resolve the issue. Wherever quoted in this paper, the primary solution stated in Table 5 has been assumed.

Two of the sources where the photometric redshift fitting using the galaxy templates does not reproduce the spectroscopic measurement are clearly quasars. Both A16 and A19 are unresolved in the NIR images, and have a quasar-like optical spectrum; thus the use of a galaxy continuum template in HYPERZ

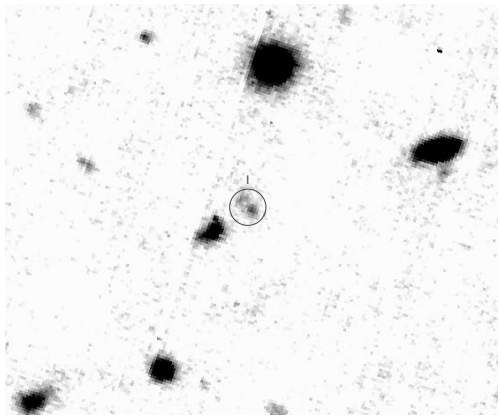

Figure 10. *CFHT I*-band image of A17 showing a double structure. In addition, there is confusion with the neighbour to the south-east in the *B*- and the *R*-band images, where the seeing is much worse. The image side is 30-arcsec long; north is to the top, and east to the left.

is unlikely to work. We have instead attempted to use various combinations of galaxy and mean QSO spectrum, but without much success. The absence of any broad-band spectral breaks creates a very large degeneracy in photometric redshift space. Our best unobscured-quasar fit to A16 yields a spectrum at a redshift of 1.35, compared to the measured redshift of 1.6 (Table 5). Given that quasars are variable, comparison of magnitudes in different bands may well be flawed. We note that A19 appears to fit into the class of objects identified by Maiolino et al. (2001) which have blue optical colours and moderate X-ray absorption. The reduced absorption due to dust compared to that expected from the gas column density suggests that such AGN have dust-to-gas ratios very different from Galactic values.

Part of the redshift mismatch for A17 is due to its proximity to a bright neighbour about 3 arcsec to the south-east (Fig. 10). A small aperture (2.7-arcsec diameter) was used to extract the flux, but the source is not well resolved from its neighbour in the *B*- and *R*-band data due to the very poor seeing at the time of the observations. Thus the *B*- and *R*-band magnitudes may be inaccurate due to contamination from the neighbour and loss of source flux outside the small aperture. The source and its neighbour are well resolved in both the UKIRT and CFHT observations; in addition, the *I*- and *H*-band images show the source itself to have a second component ~ 1 arcsec to the north-east (Fig. 10). This second component is probably too faint to be a serious source of contamination to the observed magnitudes. We speculate that the small NE component could be an extended (~ 8 kpc from the source) cloud of emission-line gas associated with the source. If it were at the same redshift as the source of $z_{\rm spec}$, then strong line emission from [O II] and [N II] and/or Hα could account for this feature showing up only in the *I* and *H* bands. We note, though, that the *on-source* spectrum of Cowie et al. (2001) – which may well not include this NE component – does not show strong [O II], and any [O III] line emission from this would emerge in the *J* band.

We note that the χ^2 values for some of the fits are much less than 1. This is due primarily to relatively shallow photometric limits (e.g., the DSS) and poor seeing conditions. Since the optical spectra are not flux-calibrated, it is not possible to compare models as output by HYPERZ with the observed spectra directly. However, the estimates of the redshifts themselves agree with the spectroscopic values in five of the eight sources as mentioned, out to a redshift of 1.7. It is usually the presence of the large Balmer break (for example, between the *R* and the *J* bands in A18; Fig. 8) – larger than the photometric uncertainties/limits – which decides the $z_{\rm phot}$ of these sources, except in the case of A20, where an additional AGN component is required.

2.4.1 A15 at $z \sim 2.8$

A15 is the highest (photometric) redshift object in our sample, and the one most strongly lensed by the cD galaxy. It is detected in very deep ISOCAM exposures at 6.75- and 15-μm (Altieri et al. 1999; fluxes published in Lémonon et al. 1998). The large $B-K$ lower limit of 5 makes this a candidate extremely red object (ERO), and this is confirmed by the deeper photometry of Cowie et al. (2001) The absence of any optical emission lines (given $z \sim 2.8$, the C III] line is expected to lie in the observed spectrum), the possibly large column density inferred from X-rays (see next section) and red optical–IR colours indicate that it is the light from the galaxy which dominates the broad-band magnitudes. Thus the photometric redshift fit should not be confused by any AGN contribution. The large $J-H$ break (Fig. 2) is best associated with the 4000-Å feature observed in early-type galaxies, placing this object at $z \sim 2.8$. We note that Lémonon et al. also quote optical, *J* and K' fluxes for this source. However, it is the addition of the *H*-band flux which produces the sharp break, and thus fixes the photometric redshift. Moreover, the colour $J-K'=2$ according to Lémonon et al. is bluer than that observed either by us ($J-K>2.9$) or by Cowie et al. using independent data sets and telescopes. We do not have an explanation for this (a difference in filter sets is not the cause), and, in the absence of more information on the photometry (the relevant reference quoted in Lémonon et al. is not published as far as we know), we continue to use the consistent set of (optical/NIR) photometry and limits as measured by us.

What is the origin of the mid-IR emission? At $z \sim 2.8$, the 6.75-μm wavelength corresponds to the *H* band in the rest frame, making it feasible that there be some starlight contribution to this radiation. Indeed, HYPERZ fits to the optical–NIR (i.e., up to, and including, *K*) predict most of the 6.75-μm flux to be starlight. The 15-μm wavelength, however, corresponds to 4 μm in the rest frame which may be strongly contaminated by dust emission, and so it was not included in the photometric redshift fitting. Thus, in HYPERZ, we fit template spectra to observations from the *B*- to the 6.75-μm bands as being due to starlight (Fig. 9).

As for the origin of the 15-μm flux, this is modelled (in conjunction with a SCUBA upper limit; Fabian et al. 2000) as due to radiation absorbed in the optical–ultraviolet regime and re-emitted at longer wavelengths. This was done using DUSTY (Ivezić, Nenkova & Elitzur 1999), and is shown as the solid line in the mid- to far-IR region in Fig. 11. Given a central source emitting power-law radiation (for example), and the density, composition, amount and optical depth of surrounding dust, DUSTY calculates a scaled radiative-transfer solution for different dust temperatures. This spectrum in Fig. 11 has been redshifted to $z=2.8$ (as obtained by HYPERZ above) and has been normalized to the 15-μm flux. This model has a dust temperature ($T_{\rm in}$) of 1500 K at the inner-dust radius, and an optical depth (τ) of 40 at 0.3 μm, with dust extending from $r_{\rm in}=0.1$ pc (pc) out to $r_{\rm out}=50$ pc from the nucleus (see WFG for more discussion on DUSTY modelling; the model presented in Fig. 11 is based on a new redshift determination, although the methodology is the same as in WFG). With an intrinsic optical (2500 Å):X-ray (2 keV) monochromatic spectral index $\alpha_{\rm ox}=1.3$, this value is in good agreement with that found by

Elvis et al. (1994) for low-redshift, bright X-ray-selected QSOs with little ultraviolet obscuration.

It is the large 15:850-μm flux limit which suggests the presence of dust which is at least hotter than characteristic SCUBA temperatures. In addition, the X-ray spectra (next section) suggest the presence of large obscuring columns (typically $10^{22}-10^{23}\,\mathrm{cm}^{-2}$ in many sources) which correspond to τ of 10–100 for Galactic dust:gas ratio. Such optical depths require medium-to-high temperatures in order to not overpredict the SCUBA upper-limit. Temperatures lower than 1500 K are certainly feasible. For example, a model with $(T_{\rm in}, \tau, r_{\rm out}/r_{\rm in}) = (500, 10, 5)$ is consistent with the data, but such models predict yet higher output in the ∼100-μm regime. However, temperatures as low as 200 K begin to overpredict observed fluxes (in the optical–IR and/or submm) for all regions of parameter space. On the other hand, inner-dust temperatures higher than 1500 K are unphysical due to sublimation of dust grains. Thus, although we cannot constrain the temperature completely, these data strongly suggest the presence of warm-to-hot dust obscuring a central AGN, with most of the power being reprocessed to the far-IR. We eagerly await missions such as *SIRTF* (Brandl et al. 2000), which will have the sensitivity required to constrain the dust temperature.

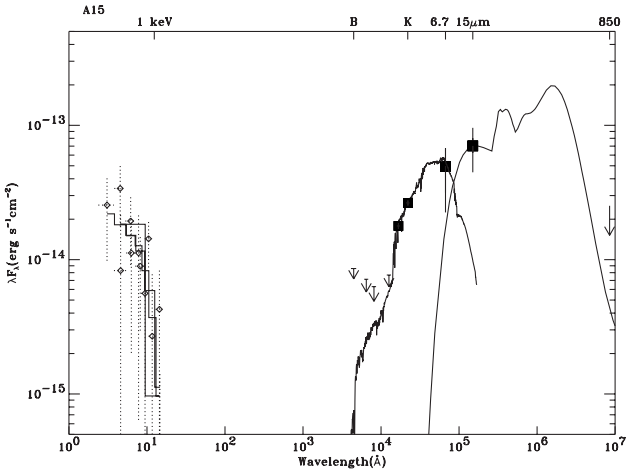

Figure 11. The total spectral energy distribution for A15. The X-ray data are marked by open diamond markers with error bars. Our optical and near-infrared values and limits are marked as solid squares. The best-fitting model for the X-ray spectrum (see Table 6) is shown as a solid line, and the other solid lines show the fits obtained in HYPERZ (optical to 6.7 μm) and DUSTY (normalized to the 15-μm flux; see text for details). The SCUBA upper limit is shown as the arrow at 850 μm. Errors are 1σ.

2.5 X-ray spectra

We attempted to extract and model the X-ray spectrum of those serendipitous sources for which a redshift (either spectroscopic or a photometric estimate) was available. The fitting was performed in XSPEC (Arnaud 1996). In practice, we can extract a usable spectrum only for the brighter sources (A6, A15, A16, A18, A19, A20, A24 and A26). We fit the model to the data only between 0.3 and 7 keV, and the spectra were grouped to have a minimum of 20 counts in each bin. In all cases we assumed the source to have a power-law spectrum with possible intrinsic absorption, i.e., in excess of the Galactic column density. We let both the power-law slope (Γ) and the excess $N_{\rm H}$ vary freely; we also repeated the fit with Γ fixed at 2. We present the results in Table 6; unless otherwise noted, the data from both observations were fitted simultaneously. Due to the small number of counts available for each source, the fits are poorly constrained. Two further sources had too few counts to fit their spectra properly, but we note that most of the counts from A28 lie between 0.7 and 0.8 keV, and that the spectra of A8 appeared to be consistent with no intrinsic absorption, for a power-law model with $\Gamma = 2$ fixed.

Table 6. Fits to the X-ray spectra of the brighter sources.

Source	Γ	$\Delta N_{\rm H}$ ($10^{22}\,\mathrm{cm}^{-2}$)	Reduced χ^2 (d.o.f.)	L(2–10 keV) ($10^{44}\,\mathrm{erg\,s}^{-1}$)	Notes
A6†	$2.1^{+1.0}_{-0.6}$	<0.61	0.77 (13)	9.2	
	[2]	<0.62	0.68 (14)	9.0	
A15	$1.7^{+2.0}_{-1.4}$	$17.5^{+60}_{-17.5}$	0.65 (9)	13.0*	
	[2]	$21.9^{+36}_{-14.6}$	0.60 (10)	17.0*	
A16	$1.3^{+2.6}_{-1.3}$	$0.2^{+12.8}_{-0.16}$	0.96 (6)	2.9	
	[2]	$3.8^{+8.0}_{-3.8}$	0.92 (7)	3.9	
A18	$3.2^{+1.3}_{-0.5}$	34.7^{+20}_{-14}	0.57 (11)	60.0*	
	[2]	$20.4^{+7.1}_{-5.2}$	0.81 (12)	20.0*	
A19	$2.31^{+0.5}_{-0.4}$	$2.6^{+2.1}_{-1.6}$	0.91 (19)	13.0	
	[2]	$1.6^{+1.2}_{-1.0}$	1.05 (20)	11.4	
A20	$1.2^{+0.2}_{-0.3}$	$1.5^{+0.9}_{-0.6}$	0.53 (30)	1.0	
	[2]	$2.7^{+0.7}_{-0.6}$	0.71 (31)	1.0	
A24	$1.3^{+3.8}_{-1.7}$	$1.8^{+4.9}_{-1.8}$	0.60 (8)	0.1	fit to 800008 data only
	[2]	$2.9^{+2.6}_{-1.4}$	0.57 (9)	0.1	fit to 800008 data only
A26	$4.2^{+5.8}_{-2.3}$	$3.9^{+12}_{-3.9}$	0.92 (2)	4.8	fit to 800009 data only
	[2]	<1.9	1.42 (3)	3.0	fit to 800009 data only

L(2–10 keV) is the unabsorbed 2–10 keV luminosity.
A square bracket around the value of Γ in column 2 denotes that the parameter was fixed at this value.
†The count rates for A6 (see Table 1) suggest the source is softer in the 800009 observation. Separate spectral fits to each spectrum suggest that this may be due to a change in $N_{\rm H}$, but since the errors on the separate fits overlap, we present the results here only for joint fitting.
*Sources A15 and A18 lie behind the cluster, and the luminosities listed are not corrected for the magnification factors of 7.8 and 2.1 respectively (Cowie et al. 2001).

The best fits to the spectra of A18, A19 and A20 are shown in Fig. 12, demonstrating that A18 and A20 require substantial amounts of excess absorption, whereas A19 does not. The contours of confidence for the values of freely fitting parameters $N_{\rm H}$ and Γ in the fits to A15, A18, A19 and A20 spectra are shown in Fig. 13. These show that the conclusion of excess absorption is robust for A18, A19 and A20 (though less so for A15) for all reasonable values of Γ. Note that the intrinsic absorption $N_{\rm H}$ inferred from the X-ray spectra is in all cases more than that implied by the moderate amounts of reddening A_V (Table 5) found from the photometric redshift fitting in the previous section. However, any reddening of the host galaxy is due to dust within the galaxy, whereas the line of sight to an active nucleus is expected to pass through additional absorption much closer in to the central engine.

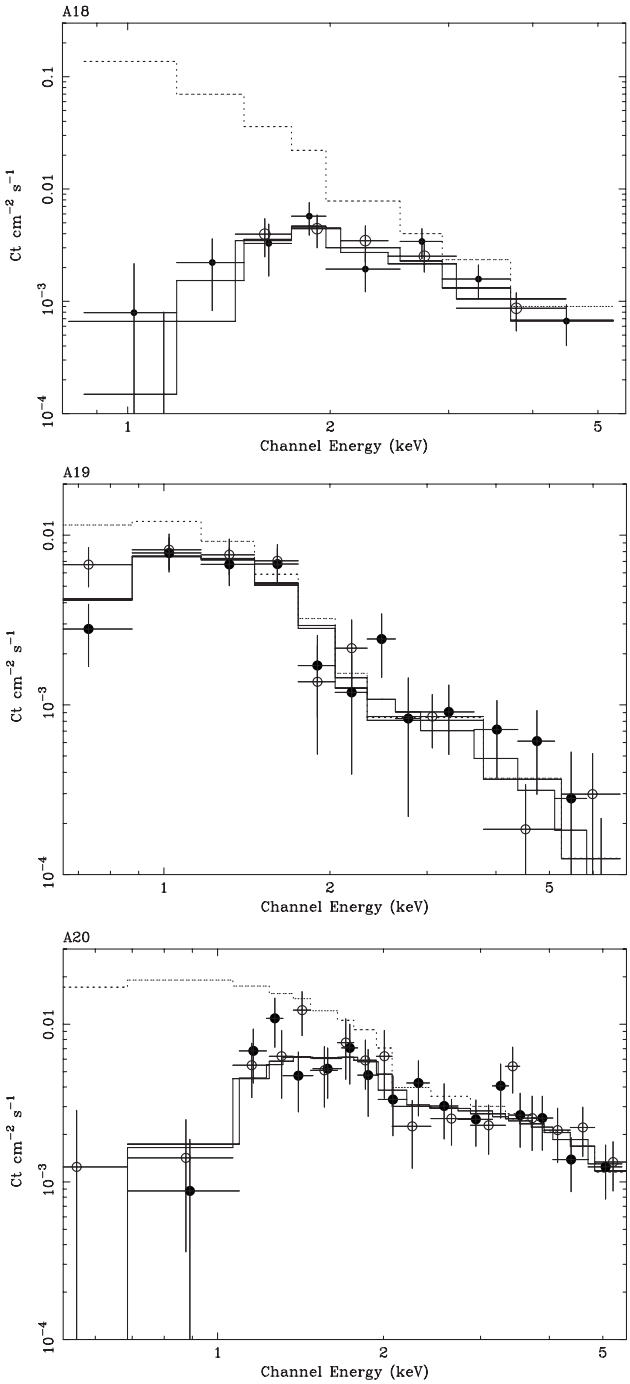

Figure 12. The X-ray spectra of A18, A19 and A20, showing the best-fitting absorbed power-law models to the data (solid line), and the fit, but now without the intrinsic absorption (dotted line). The parameters of these best-fitting models are given in Table 6. The solid and open circle markers indicate the spectrum extracted for the source from the two different data sets.

It is also possible to examine the faint sources which do not have enough counts to justify spectral fitting. We used XSPEC to predict the soft-to-hard (S/H) ratio that would be observed (on the I3, S2, S3 and S4 chips) for an absorbed (intrinsic + Galactic) power-law source placed at a range of redshifts with a variety of intrinsic column densities (cf. table 4 in Crawford et al. 2001 for a similar table, though with zero Galactic absorption). Next, the observed S/H ratios (Table 1) for sources with a redshift determination were compared with the predicted values, from the same chip, in order to constrain the intrinsic column densities. These are listed in Table 7. Predictions were made for power-law indices Γ of 1.4 and 2, and it appears that some level of intrinsic absorption is possible for sources A4, A12, A14 and A27. Note that the maximum observable S/H ratio for a fixed photon index will be from an intrinsically unabsorbed source. Any intrinsic absorption depletes only the soft counts and thus decreases the S/H ratio. This is the basis of the predictions of larger Γ in the last column of Table 7 for the very soft sources (with observed S/H greater than the predicted maximum for $\Gamma = 2$ and for $\Gamma = 1.4$). It is not possible to constrain the intrinsic absorption in these cases, since larger photon indices could also imply larger column densities.

3 DISCUSSION

We have detected 31 serendipitous sources in two separate *Chandra* observations of the cluster A 2390. The majority of these (18 in total) were detected on the ACIS-S3 chip, which contains the pointing target of the observations. We do not believe that this concentration is due to weak gravitational lensing by the cluster, as other effects such as the degradation of the PSF and vignetting make the other chips less sensitive to faint sources. Only three of the sources are sufficiently close to the line of sight through the centre of the cluster potential to be significantly magnified by gravitational lensing. These are A15, A17 and A18, which are magnified by 7.8, 2.8 and 2.1 respectively (Cowie et al. 2001). None of the sources appears significantly more extended than the PSF expected at that position on the detectors, and hence all are consistent with being point sources. About 50 per cent of the sample have soft X-ray spectra (S/H $>$ 3), and about one-third of the sources show hard spectra (i.e., S/H $<$ 2). The six sources with the hardest colours (S/H $<$ 1.5) are A2, A15, A18, A20, A24 and A30. Eight of the sources showed evidence for variability on an 11-month time-scale. The 0.5–7 keV fluxes of the sources range from just below, to a few times above, 10^{-14} erg cm^{-2} s^{-1}.

We are particularly interested in the optically fainter sources in our sample that also show the hardest X-ray colours, as these are possible prototypes for the sources contributing to the hard XRB. Standard models for the synthesis of the hard X-ray background (Setti & Woltjer 1989; Wilman & Fabian 1999; Wilman et al. 2000b) predict such sources to be heavily obscured AGN at redshifts greater than one. To this end, we have fitted an absorbed power-law model to simple X-ray spectra of the eight sources with sufficient counts and a known redshift. The unabsorbed (de-magnified) 2–10 keV luminosity ranges from 0.1×10^{44} to 30×10^{44} erg s^{-1}. The intrinsic absorption required varies from

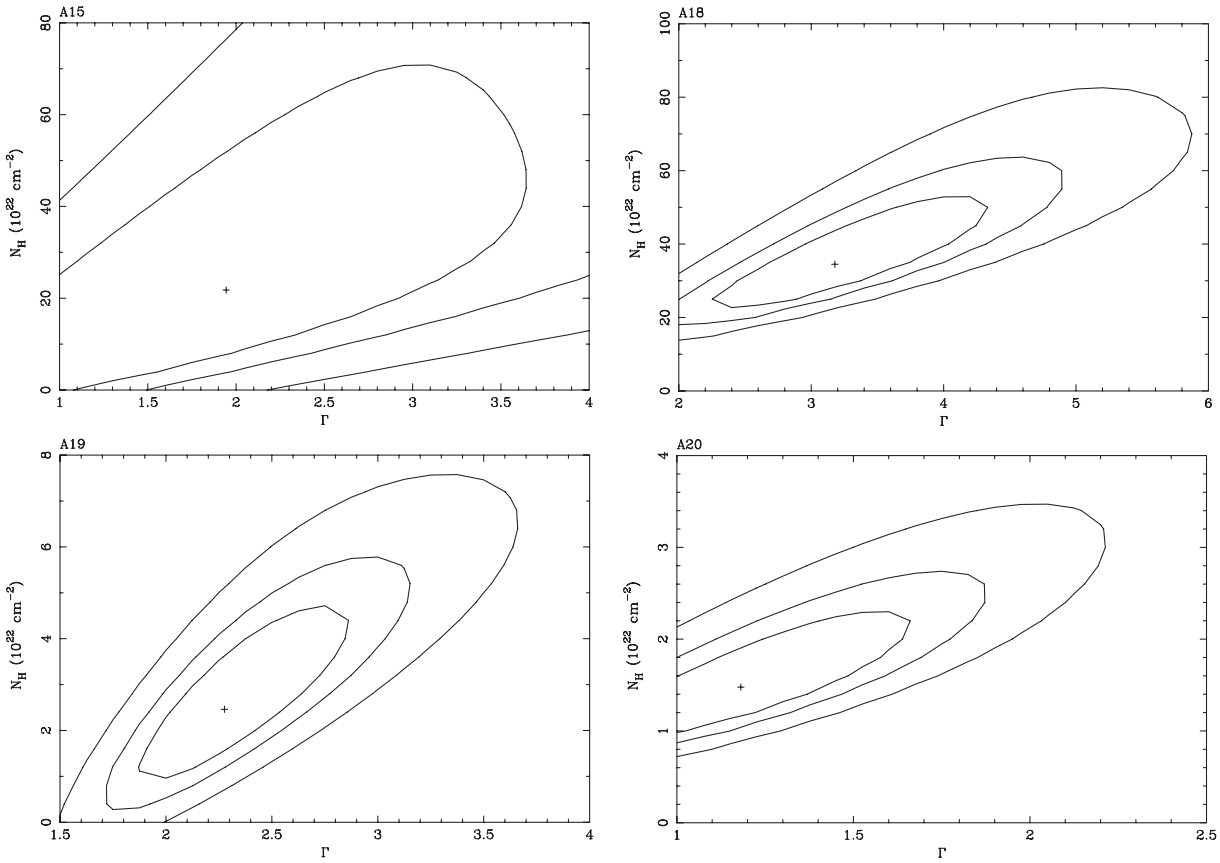

Figure 13. The confidence contours on the parameters Γ and intrinsic absorption N_H for the X-ray spectral fits to A15, A18, A19 and A20.

Table 7. Absorbed-powerlaw-model-predicted intrinsic columns (above Galactic absorption) or photon indices from the observed S/H ratio for sources with insufficient counts for spectral fitting.

Source	Redshift	S/H ratio	Prediction[1]
A4	1.2172	>1.89	$N_H < 5$ [2.0]
			$N_H < 0.5$ [1.4]
A8	0.8030	>4.71‡	$N_H < 0.1$ [2.0] and $\Gamma > 1.4$
A10	0.2242	>31.26	$\Gamma > 3$
A12[2]	2.28	2.03 ± 1.1	$1 < N_H < 30$ [2.0]
			$N_H < 20$ [1.4] or* $\Gamma > 1.4$
A12[2]	0.66	2.03 ± 1.1	$0.2 < N_H < 4$ [2.0]
			$N_H < 2$ [1.4] or* $\Gamma > 1.4$
A13	1.5933	>5.9	$\Gamma > 2$
A14	1.35	>2.20	$N_H < 5$ [2.0] and $\Gamma > 1.4$
A17	1.466	>4.42†	$N_H < 0.5$ [2.0] and $\Gamma > 1.4$
A27	0.87	2.23 ± 1.0†	$0.7 < N_H < 4$ [2.0]
			$N_H < 2$ [1.4] or* $\Gamma > 1.4$
		6.45 ± 2.6‡	$N_H < 0.4$ [2.0] or* $\Gamma > 2.0$
A28	1.0330	4.38 ± 2.1†	$N_H < 2$ [2.0] or* $\Gamma > 2.0$
			$N_H < 0.2$ [1.4] or* $\Gamma > 1.4$

Redshifts stated to four decimal places are spectroscopic, and the rest are photometric.

[1]The limits on the column densities (stated in units of 10^{22} cm^{-2}) account for the errors on the S/H ratio where available; otherwise, they have been constrained to the nearest half-decade. The assumed power-law indices (Γ) are stated in square brackets.

[2]The two rows correspond to the two possible photometric redshifts for this source. See Table 5 and the text.

†Obtained from the 800008 observation only.

‡Obtained from the 800009 observation only.

*These two possibilities come from the values of S/H at the extremes of the range encompassed by the S/H error. The upper limit on N_H corresponds to the lower value of S/H, and the lower limit on Γ corresponds to the higher value of S/H.

none (in two cases) to 35×10^{22} cm^{-2}. Most of these sources are thus in the Compton-thin regime. We note that the two sources for which the X-ray spectrum indicates the most intrinsic absorption ($N_H > 10^{23}$ cm^{-2}) are those – A15 and A18 – that are magnified from gravitational lensing by the foreground cluster A 2390. Without the presence of the foreground cluster we would not have been able to observe these sources so clearly. We have found no sources in this field which are clearly Compton-thick (i.e., have an absorbing column $>10^{24}$ cm^{-2}). The lack of such sources is, however, consistent with predictions of the observable density of Compton-thick objects at this flux level (Wilman & Fabian 1999). As well as its high intrinsic column density, A18 also has an intrinsic luminosity $>10^{45}$ erg s^{-1} (correcting for the gravitational lensing magnification); thus it is a good candidate for an X-ray Type-II quasar.

We have clear optical identifications for 24 of the sources, and imaged 12 in the NIR, including four of the sources with S/H < 1.5. 11 of these 12 sources were detected in *J*, *H* and *K*. The remaining source (A15), not detected down to faint optical levels and in the *J* band, has a large $J - H$ break. Its colour $R - K > 4.4$ confirms it as an ERO (Cowie et al. 2001). The other two lensed sources, A17 and A18 are also EROs (with $R - K > 5$), and A14 has $R - K > 4.2$. Optical spectra were taken for 15 of the sources, revealing only two of them to be stars (note also that the magnitudes of A9 and its stellar profile in the DSS strongly suggest that this source is also a star). The majority of the sources show AGN spectra at a range of line luminosities; half show broad lines and the others are narrow-line AGN. This concurs with a large fraction of the sources showing X-ray variability. Two of the sources – A16 and A19 – are clearly quasars from their optical

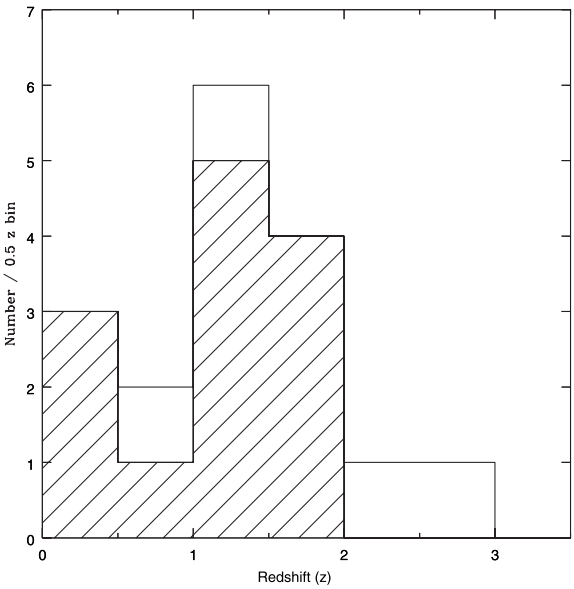

Figure 14. The redshift distribution, where known, of the serendipitous sources in the field of A 2390. The shaded boxes indicate those sources that have a spectroscopic redshift rather than a photometric redshift.

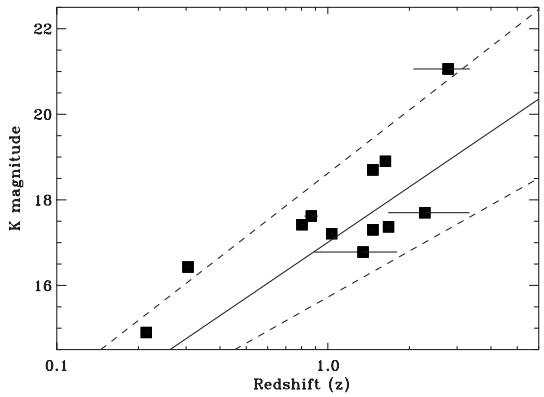

Figure 15. The $K-z$ relation for our sources. The solid line shows the $K-z$ relation for radio galaxies, and the dotted lines indicate the scatter of the radio galaxies about this line (taken from Eales et al. 1993). The K magnitudes of A15, A17 and A18 have been corrected for the magnification due to gravitational lensing.

spectra, broad-band colours and point-like appearance in the IR images. Apart from the two lowest redshift non-cluster objects, the rest with optical emission lines have soft X-ray spectra. Seven of the nine sources at high enough redshift (and with optical spectra) show the Mg II emission line. We note that A18 – one of the two sources with large amounts of intrinsic absorption – shows no sign of Mg II emission (although its expected position is right on the edge of the observed spectrum). The other heavily absorbed source, A15, shows no sign of C III λ1909, which should be observed at $\sim$7180 Å if the source is at the photometric estimated redshift of 2.78 (Fig. 6). We do not have sufficient counts for an X-ray spectrum for the other source that does not show Mg II emission (A8), although we note that it is a soft X-ray source (Table 1). There does not seem to be a broad component to the Balmer emission lines in A20 or in A24, which are two X-ray-hard sources, at least one of these being a narrow-line Seyfert.

We have obtained a new spectroscopic redshift for 10 sources

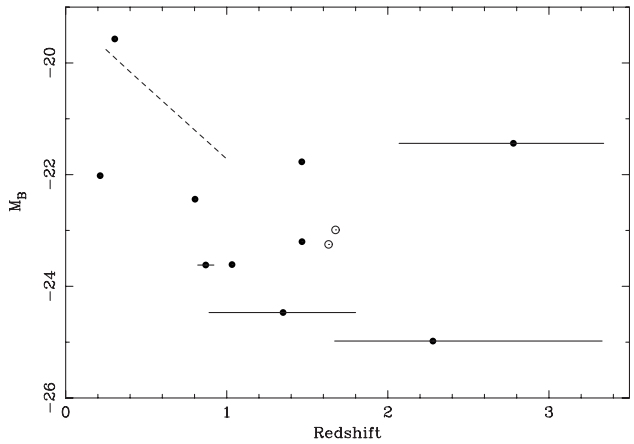

Figure 16. The absolute M_B of the host galaxies from the HYPERZ fitting plotted against redshift. The dashed line shows the magnitude–redshift relation of blue field galaxies out to $z \sim 1$ from Lilly et al. (1995). A16 and A19 are marked by open circle symbols, as their light is dominated by a quasar component.

(three others were already in the literature), and estimated a photometric redshift for a further four sources (one of which is in agreement with a previously published photometric estimate). We tested the results of photometric redshift fitting for those sources for which we also had optical spectra, and found reasonably good agreement except for the two quasars. We show the redshift distribution for all the sources in Fig. 14. One source, A10 at $z = 0.2242$, probably lies within the cluster A 2390. The four very hard X-ray sources for which we have redshifts span the whole redshift range observed, at 0.214, 0.305, 1.467 and 2.78. Of the 12 sources without either optical spectroscopy or NIR imaging, about half are probably hard (S/H < 2). Four of this hard group are undetectable on the DSS, and four have no identification.

The K magnitudes and the redshifts z for all of our sources follow the relationship known for radio galaxies (Fig. 15; Eales et al. 1993), even though none of our serendipitous sources are coincident with radio detections listed in the NASA/IPAC Extragalactic Database (NED; this area of sky is not covered by the FIRST catalogue). This result contrasts with the tendency for the *Chandra* sources found in the ELIAS survey area to lie well above the $K - z$ relation (Willott et al. 2001). The B magnitude of the host galaxies inferred from the photometric redshift fitting increases with redshift (Fig. 16). Comparison of our magnitudes to the magnitude–redshift distribution of the blue field galaxy out to $z \sim 1$ (from Lilly et al. 1995) indicates that the majority of our sources lie in brighter, and presumably more massive, galaxies than the general field popuation. None of the sources with optical spectra have their B bands biased significantly by AGN line contribution (we estimate at most 10 per cent of the total flux due to C III] in A13 and A26), although A20 does have strong lines in the R and I bands. AGN continuum contribution is harder to estimate, although this is probably an issue only for the softer sources.

4 CONCLUSIONS

We have obtained an insight into the properties of the harder, fainter population from the three gravitationally lensed sources (A15, A17 and A18). All would have been detected in X-rays without the lensing, A15 and A17 would have been just detected, and A18 well detected. A15 and A18 have hard X-ray spectra. The

magnification has made the near-infrared work easier, and Cowie et al. (2001) have obtained (similar) infrared spectroscopic redshifts ($z = 1.47$) for both A17 and A18 and a photometric redshift ($z \sim 2.6$ confirmed here) for A15. A15 and A18 appear to be genuine obscured quasars with intrinsic 2–10 keV luminosities of 2×10^{44} and 2×10^{45} erg s^{-1} respectively. They were both also detected in the mid-infrared by ISOCAM. Model spectral energy distributions for the $z \sim 2.8$ source indicate that the reprocessed radiation is emitted by hot (1500 K) or warm dust, peaking at $\sim 100\,\mu$m.

The results of our modest sample are consistent with, and extend, previous work on deeper fields (e.g. Barger et al. 2001). The majority of the sources for which we have optical spectra show broad-line emission, similar to results from other X-ray surveys in previous missions (e.g. Lehmann et al. 2001). We find that (i) most of the sources at 0.5–7 keV fluxes around 10^{-14} erg cm^{-2} s^{-1} can be optically identified, although deep optical and infrared imaging is required; (ii) about half of the sources, mostly the X-ray softer ones, have optical emission lines with which spectroscopic redshifts can be obtained; (iii) photometric redshifts work well and enable some more redshifts to be obtained, particularly of harder sources, and (iv) about one-third of the sources are both optically faint and hard. These last sources are likely to be important for producing the harder parts of the XRB, which peaks in νI_ν at ~ 30 keV, although the class of faint Compton-thick sources which should dominate at the peak may not yet have been detected. If A15 is typical of the optically faint hard sources, then they are obscured quasars in early-type bulges at redshifts of 2–3, or possibly higher. The absorbed X-ray and UV emission emerges in the mid- to far-infrared.

ACKNOWLEDGMENTS

We are grateful to the referee for careful reading of the manuscript and constructive comments which have improved and clarified the paper. We thank the *Chandra* project for the X-ray data, and M. Bolzonella, J.-M. Miralles and R. Pelló for making HYPERZ available. We also thank Stefano Ettori for the use of his software in reducing the X-ray data, and Andrew Firth for his help with HYPERZ. CSC and ACF thank the Royal Society, PG thanks the Isaac Newton Trust, the Overseas Research Trust and Fitzwilliam College Trust Fund, and RJW thanks the PPARC for financial support. Support for AJB was provided by NASA through the Hubble Fellowship grant HF-01117.01-A awarded by the Space Telescope Science Institute, which is operated by the Association of Universities for Research in Astronomy, Inc., for NASA under contract NAS 5-26555. AJB and LLC acknowledge support from NSF through grants AST-0084847 and AST-0084816 respectively.

The United Kingdom Infrared Telescope is operated by the Joint Astronomy Centre on behalf of the UK Particle Physics and Astronomy Research Council. This research made use of data obtained from the Isaac Newton Group Archive at the UK Astronomy Data Centre, Cambridge, and the Canadian Astronomy Data Center, which is operated by the Dominion Astrophysical Observatory for the National Research Council of Canada's Herzberg Institute of Astrophysics, and has also made use of the NASA/IPAC Extragalactic Database (NED), and the Digitized Sky Surveys which were produced at the Space Telescope Science Institute under U. S. Government grant NAG W-2166.

REFERENCES

Allen D. A., 1976, MNRAS, 174, 29P
Allen S. W., Ettori S., Fabian A. C., 2001, MNRAS, 324, 877
Altieri B. et al., 1999, A&A, 343, L65
Arnaud K. A., 1996, in Jacoby G., Barnes J., eds, ASP Conf. Ser. Vol. 101, Astronomical Data Analysis Software and Systems V. Astron. Soc. Pac., San Francisco, p. 17
Barger A. J., Cowie L. L., Mushotzky R. F., Richards E. A., 2001, AJ, 121, 662
Bolzonella M., Miralles J.-M., Pello R., 2000, A&A, 363, 476
Brandl B. et al., 2000, in Montmerle T., Andre P., eds, ASP Conf. Ser., From Darkness to Light. Astron. Soc. Pac., San Francisco in press (astro-ph/0007300)
Brandt W. N. et al., 2001, AJ, 122, 1
Bruzual G. A., Charlot S., 1993, ApJ, 405, 538
Calzetti D., Armus L., Bohlin R. C., Kinney A. L., Koornneef J., Storchi-Bergmann T., 2000, ApJ, 533, 682
Coleman G. D., Wu C.-C., Weedman D. W., 1980, ApJS, 43, 393 (CWW)
Comastri A., Setti G., Zamorani G., Hasinger G., 1995, A&A, 296, 1
Cowie L. L. et al., 2001, ApJ, 551, L9
Crawford C. S., Fabian A. C., Gandhi P., Wilman R. J., Johnstone R. M., 2002, MNRAS, 324, 427
Eales S. A., Rawling S., Dickinson M., Spinrad H., Hill G. J., Lacy M., 1993, ApJ, 409, 578
Elvis M. et al., 1994, ApJS, 95, 1
Epps H. W., Miller J. S., 1998, Proc SPIE, 3355, 48
Fabian A. C. et al., 2000, MNRAS, 315, L8
Giacconi R. et al., 2001, ApJ, 551, 624
Granato G. L., Danese L., Franceschini A., 1997, ApJ, 485, 147
Hasinger G. et al., 1998, A&A, 329, 482
Hornschemeier A. E. et al., 2001, ApJ, 554, 742
Ivezić Z., Nenkova M., Elitzur M., 1999 (astro-ph/9910475)
Lehmann I. et al., 2001, A&A, 371, 833
Lémonon L., Pierre M., Cesarsky C. J., Elbaz D., Pello R., Soucail G., Vigroux L., 1998, A&A, 334, L21
Lilly S. J., Tresse L., Hammer F., Crampton D., Le Fèvre O., 1995, ApJ, 455, 108
Madau P., Ghisellini G., Fabian A. C., 1994, MNRAS, 270, L17
Maiolino R., Marconi A., Salvati M., Risaliti G., Severgnini P., Oliva E., La Franca F., Vanzi L., 2001, A&A, 365, 28
Mushotzky R. F., Cowie L. L., Barger A., Arnaud K. A., 2000, Nat, 404, 459
Setti G., Woltjer L., 1989, A&A, 224, L21
Stark A. A., Gammie C. F., Wilson R. W., Bally J., Linke R. A., Heiles C., Hurwitz M., 1992, ApJS, 79, 77
Tozzi P. et al., 2001, ApJ, 562, 42
Willott C. J. et al., 2001 (astro-ph/0105560)
Wilman R. J., Fabian A. C., 1999, MNRAS, 309, 862
Wilman R. J., Fabian A. C., Gandhi P., 2000, MNRAS, 318, L11 (WFG)
Wilman R. J., Fabian A. C., Nulsen P. E. J., 2000, MNRAS, 319, 583
Yee H. K. C. et al., 1991, A&AS, 88, 133

This paper has been typeset from a TEX/LATEX file prepared by the author.